Applied Clay Science 276 (2025) 107942

Contents lists available at ScienceDirect

Applied Clay Science

journal homepage: www.elsevier.com/locate/clay

Research Paper

Protoporphyrin-grafted halloysite nanotubes for boosted photodynamic activity in chitosan nanocomposite films

Marina Massaro [a], Federica Leone [a], Angelo Nicosia [b], Giuseppe Lazzara [c], Giuseppe Cavallaro [c], Grazia M.L. Messina [b], César Viseras [d,e], Rita Sánchez-Espejo [d], Monica Notarbartolo [a], Roberta Puglisi [b], Placido G. Mineo [b], Raquel de Melo Barbosa [f], Serena Riela [b,*]

[a] Dipartimento di Scienze e Tecnologie Biologiche, Chimiche e Farmaceutiche (STEBICEF), Università di Palermo, Viale delle Scienze, Parco d'Orleans II, Ed. 16-17, 90128 Palermo, Italy
[b] Dipartimento di Scienze Chimiche (DSC), Università di Catania, Viale Andrea Doria 6, 95125 Catania, Italy
[c] Dipartimento di Fisica e Chimica E. Segrè (DiFC), Università di Palermo, Viale delle Scienze, Parco d'Orleans II, Ed. 17, 90128 Palermo, Italy
[d] Department of Pharmacy and Pharmaceutical Technology, Faculty of Pharmacy, University of Granada, Campus Universitario de Cartuja, 18071 Granada, Spain
[e] Andalusian Institute of Earth Sciences, CSIC-UGR, 18100, Armilla, Granada, Spain
[f] Department of Pharmacy and Pharmaceutical Technology, School of Pharmacy, University of Seville, C/Professor García González 2, 41012 Sevilla, Spain

ARTICLE INFO

Keywords:
Chitosan
Halloysite
Covalent modification
Photodynamic therapy

ABSTRACT

Chitosan-based materials are widely explored for biomedical applications due to their biocompatibility, biodegradability, and excellent film-forming ability. In this work, we report the development of hybrid chitosan films reinforced with halloysite nanotubes (Hal) covalently functionalized with protoporphyrin IX (PPIX), aiming to enhance their photodynamic properties. Photodynamic therapy (PDT) has emerged as a promising and minimally invasive technique for cancer treatment due to its selectivity and low toxicity. However, the clinical use of many photosensitizers, such as PPIX, is limited by their poor solubility in water. The covalent anchoring of PPIX onto the external surface of Hal significantly improved its availability in water, which was further enhanced upon coordination with Zn^{2+} ions. The resulting Hal-PPIX nanomaterials were characterized by spectroscopic and microscopic techniques and evaluated, both chemically and biologically, for their ability to generate reactive oxygen species (ROS) under visible light irradiation. As proof of concept, the nanomaterials were incorporated into chitosan films and studied for their mechanical properties and AFM was employed to investigate the surface morphology of them. The results demonstrate the potential of these bio-based nanocomposites as promising candidates for topical photodynamic therapy, particularly in skin cancer treatment.

1. Introduction

Polysaccharide-based materials have gained increasing interest in biomedical applications due to their inherent biocompatibility, biodegradability, and structural versatility (Jabeen and Atif, 2024). Among these, chitosan, a cationic polysaccharide derived from chitin, has been widely investigated for its film-forming ability, mucoadhesiveness, and functionalization potential, making it a valuable platform for developing nanocomposite biomaterials. Indeed, chitosan is a biodegradable polymer that has been widely used in drug delivery systems (Nikezić et al., 2020). In the field of pharmaceutical nanotechnology, it has been used as a polymer of polymeric particles and as a surface coating for different drug delivery systems. To improve physico-chemical properties of chitosan, different nanocomposite materials have been developed which have found applications in different biomedical fields (Khan et al., 2020; Yadav et al., 2023). Recently, Moreira Lira et al. reported the synthesis of chitosan based nanostructured lipid carriers containing chloroaluminum phthalocyanine, as a photosensitizer, for skin cancer treatment that shown promising photodynamic efficiency in melanoma cell culture (Almeida et al., 2022).

Recent advances in nanotechnology have demonstrated that the incorporation of inorganic nanofillers into chitosan matrices can significantly improve their mechanical, barrier, and biological properties (Moura et al., 2016; Silva et al., 2021). In particular, clay minerals, which are phyllosilicates with nanometric dimensions, have been used in healthcare since ancient times due to their intrinsic properties,

* Corresponding author.
E-mail address: serena.riela@unict.it (S. Riela).

https://doi.org/10.1016/j.clay.2025.107942
Received 29 April 2025; Received in revised form 22 July 2025; Accepted 22 July 2025
Available online 1 August 2025

making them one of the most promising materials (Moura et al., 2016; Peixoto et al., 2021). Among them, halloysite (Hal) with a general formula of $Al_2Si_2O_5(OH)_4{\cdot}nH_2O$, typically found in hollow tubular structures in the nanometric range, represents a particularly attractive class of nanofillers (Bao et al., 2024; Thomas et al., 2024). In this context, Lazzara et al. reported that the interaction of Hal with a biopolymers is driven by the polymer charge; in particular, chitosan being positive mainly interacts with the clay external surface, thus embedding it, while a negative polymer such as alginate, interacts with the positive Hal lumen (Bertolino et al., 2016).

Due to the presence of an empty lumen and tuneable surface chemistry, Hal hold great potential as carriers for biomedical applications (Massaro et al., 2022c). Indeed, the empty lumen can be loaded with several hydrophobic biologically active compounds, which benefit from slow and sustained release over the time (Boraei et al., 2024; Husain et al., 2023; Massaro et al., 2023; Yanamadala et al., 2023). Additionally, Hal are biocompatible materials capable of crossing cellular membranes, and localizing themselves in the perinuclear region, and in some cases, depending on modifications, the cellular nuclei as well (Falanga et al., 2024). Due to their above properties, Hal has emerged as versatile carriers in drug delivery and tissue engineering (Feng et al., 2024). To further increase functionality, covalent modification of the silanol groups on the external surface of Hal, with a variety of organic molecules, generates nanomaterials with appealing properties (Massaro et al., 2022a; Massaro et al., 2022c). Moreover, Hal with therapeutic agents allows for the development of more stable (Massaro et al., 2024a), tailored nanomaterials. Within this context, photosensitizers, such as Protoporphyrin IX (PPIX) (Izquierdo et al., 2024), are of great interest for their ability to produce reactive oxygen species (ROS) upon light activation, a mechanism exploited in photodynamic therapy (PDT) (Alea-Reyes et al., 2017; Chen et al., 2022; Nicosia et al., 2020; Penon et al., 2017; Villari et al., 2021; Yang et al., 2023). However, the clinical use of many photosensitizers, such as PPIX, is limited by their poor solubility in water and aggregation tendency, which reduces its therapeutic efficacy. Carrier systems offer an attractive solution to improve the solubility and stability of PPIX (da Silva et al., 2013; Ding et al., 2011).

While previous studies have demonstrated the potential of Hal as photosensitizer carrier (Karewicz et al., 2021; Li et al., 2019; Tan et al., 2021), covalent modification strategies remain underexplored. Herein, we report the design of chitosan-based nanocomposite films embedding Hal covalently functionalized with first PPIX alone and successively with its Zn(II) complex (Fig. 1). After synthesizing the Hal-PPIX nanomaterial, the successful modification was confirmed using several techniques, and the morphology was imaged by high-angle annular dark-field scanning transmission electron microscopy (HAADF/STEM). Furthermore, since metalloporphyrins exhibit superior biological activity compared to free-base porphyrins (Shao et al., 2019), we also investigated the interaction of PPIX with three metal ions, namely Co^{2+}, Cu^{2+} and Zn^{2+} ions, via spectrofluorimetric titrations. Subsequently, the PPIX@Zn complex was synthesized and covalently grafted onto the external surface of the suitable Hal-SH derivative. The ability of the obtained nanomaterials to generate singlet oxygen ($^1O_2$) species was evaluated chemically by monitoring the disappearance of the maximum absorption band of 1,3-Diphenylisobenzofuran under 650 nm laser irradiation, and biologically, by treating multidrug-resistant leukemia cell lines (HL60R) with the nanomaterial irradiating them with the same laser.

Finally, as a proof of concept for topical applications, these nanomaterials were incorporated into chitosan matrices, assessing their mechanical and morphological properties.

It is hypothesized that covalent integration of protoporphyrin functionalized halloysite nanotubes into a chitosan matrix will result in nanocomposite films with enhanced photodynamic activity, improved mechanical flexibility, and morphological characteristics suitable for potential application in topical cancer therapy. This study provides a novel strategy to develop chitosan-based photodynamically active films through the integration of covalently functionalized halloysite nanotubes, paving the way for future topical applications in skin cancer treatment.

2. Experimental details

2.1. Materials

Protoporphyrin IX (≥ 95%), $ZnCl_2$ (≥ 98%), $CoCl_2$ (97%), $CuCl_2$ (97%), 2-2'-azobisisobutirronitrile (AIBN) (98%), 1,3-Diphenylisobenzofuran (DPBF) (97%) and Chitosan (medium molecular weight, degree of deacetylation ≥ 75%) were purchased from Merck (Darmstadt, Germany) and used without further purification. Thiol modified halloysite (Hal-SH) was synthetized as reported elsewhere (Massaro et al., 2021).

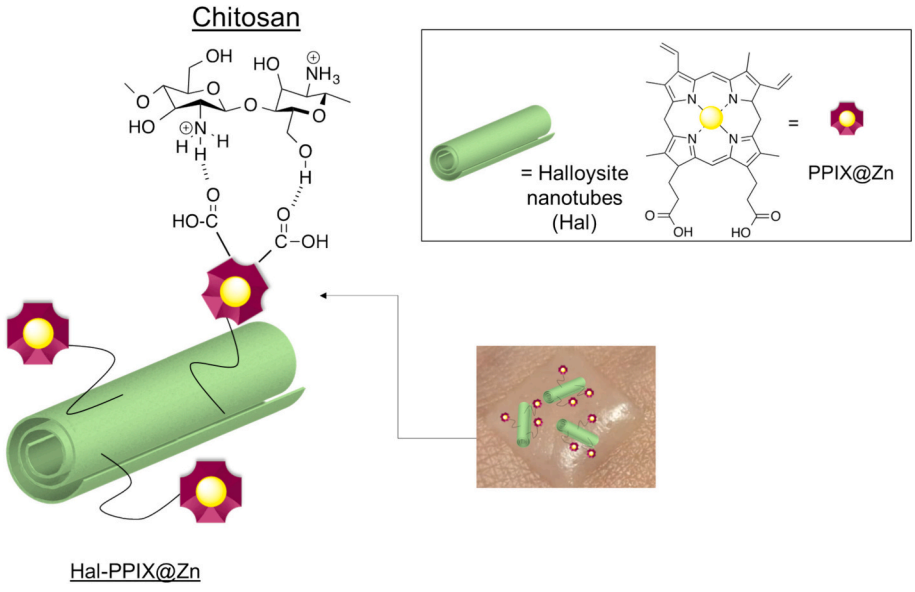

Fig. 1. Schematic representation of the developed chitosan nanocomposite reinforced with halloysite covalently linked with protoporphyrin IX.

2.2. Methods

Syntheses performed by microwave were carried out using a single-mode CEM DISCOVER system (CEM Corporation, Matthews, NC, USA) in a closed vessel.

Thermogravimetric analyses were performed with Pyris TGA7 (PerkinElmer, Waltham, MA, USA) in the temperature range of 50–800 °C (heating rate of 10 °C min^{-1}), in a nitrogen atmosphere (flow rate of 60 mL min^{-1}).

FTIR spectra (KBr) were acquired with an Agilent Technologies Cary 630 FT-IR spectrometer (Agilent Technologies, Santa Clara, CA, USA) by preparing tablets by mixing 5 mg of the sample powder with 100 mg of KBr.

UV–*vis* measurements were performed using a Beckmann DU 650 spectrometer (Beckman Coulter, Inc., Brea, CA, USA).

Steady-state fluorescence spectra were recorded using a JASCO FP-777 W spectrofluorometer (JASCO, Cremella (LC), Italy). Excitation and emission slits were set to 3 nm, with an emission interval ranging between 550 and 750 nm and an excitation wavelength of 410 nm and 420 nm.

The size analysis, ζ-potential and polydispersity index of the samples were determined using a Malvern Zetasizer Nano ZS instrument (Malvern Instruments, London, UK), fitted with a 532-nm laser at a fixed scattering angle of 173°.

Transmission electron microscopy (TEM) was performed by means of a FEI Titan G2 60–300 ultra- high-resolution transmission electron microscope (FEI, Lausanne, Switzerland) coupled with analytical electron microscopy (AEM) performed with a SUPER X silicon drift windowless energy dispersive X-ray spectroscopy (XEDS) detector. AEM spectra were saved in mode STEM (scanning transmission electron microscopy) with a HAADF (high angle annular dark field) detector.

XPS measurements were made with a SPECS SAGE HR 100 spectrometer (SPECS, Berlin, Germany) in high vacuum (10^{-7} Pa), equipped with a non-monochromatic Mg X-ray source with a Kα lines of 1253.6 eV. An electron dilution gun was used to neutralize the charge.

Atomic Force Microscopy (AFM) measurements were performed in tapping mode by using a Nanoscope IIIA-MultiMode AFM (Digital Instruments, Santa Barbara, CA, USA). The device was equipped with a < J > calibrated scanner using grating manufacturers. Images were recorded at scan rate of 1 Hz and 512 × 512 pixels per image (i.e., in high resolution conditions) by using 0.5–2 Ω·cm Phosphorous (n) doped silicon tips mounted on cantilevers with a nominal force constant of 40 N/m and a resonant frequency of 300 kHz. Throughout imaging, the set point was continuously adjusted to maintain the force at the lowest feasible value. Image analysis was carried out using DI software, version 4.23r6. The images were flattened to remove background slopes.

The tensile properties of the nanocomposite films were studied by Dynamic Mechanical Analysis (DMA) using the DMA Q800 apparatus (TA Instruments, New Castle, DE, USA). The tests were conducted under a controlled stress ramp (1 MPa min^{-1}) at 25.0 ± 0.1 °C.

2.3. Synthesis of Hal-PPIX via MW irradiation

Hal-SH (150 mg) and PPIX (70 mg), were homogenized and introduced into a microwave tube provided with a cup. The mixture was inserted in the MW apparatus at 100 °C, under constant stirring, for 10 min at initial power of 80 W, in the presence of a catalytic amount of AIBN. Successively, the solid was washed several times with DMF, methanol and CH_2Cl_2 and finally dried at 60 °C under vacuum.

2.4. Synthesis of Hal-PPIX via UV irradiation

In a quartz test tube, Hal-SH (150 mg) and PPIX (70 mg) were dissolved in methanol. A stream of Ar was bubbled through the solution for 15 min to thoroughly degas it. The test tube was placed in front of an Hg lamp (265 nm) and stirred overnight at r.t. conditions. The obtained powder was washed several times with THF, methanol and CH_2Cl_2 and finally dried at 60 °C under vacuum.

2.5. Interaction of Hal-PPIX nanomaterial with metal ions

The interaction between Co^{2+}, Zn^{2+} and Cu^{2+} ions and Hal-PPIX nanomaterial was studied by spectrophotometric titration using fluorescence spectroscopy at two different temperatures (20 °C and 37 °C). To a methanol dispersion of Hal-PPIX (0.1 mg mL^{-1}, 10 mL), increasing volumes (0–750 μL) of an aqueous Co^{2+}, Zn^{2+} or Cu^{2+} ions solution (10^{-4} M) were added. Spectra were acquired in wavelength intervals ranging between 550 and 750 nm at $\lambda_{ex} = 410$ nm.

2.6. Synthesis of PPIX@Zn

To a solution of PPIX (200 mg, 0.36 mmol, 1 eq.) in (50 mL) a solution of $ZnCl_2$ (480 mg, 3.6 mmol, 10 eq.) in DMF (10 mL) was added. The mixture was stirred overnight at 65 °C. After distilling under reduced pressure, washing with water and methanol by centrifuged, the obtained solid was dried under vacuum condition.

2.7. Synthesis of Hal-PPIX@Zn

Hal-SH (150 mg) and PPIX@Zn (70 mg) were homogenized and introduced into a microwave tube provided with a cup. The vial was inserted in the MW apparatus at 100 °C, under constant stirring, for 10 min at initial power of 80 W, in the presence of a catalytic amount of AIBN. Successively, the solid was washed several times with DMF, methanol and CH_2Cl_2 and finally dried at 60 °C under vacuum.

2.8. Singlet oxygen generation

The singlet oxygen quantum yield of Hal-PPIX and Hal-PPIX@Zn nanomaterials were determined using an indirect detection technique. The generation of ROS was evaluated by using diphenylisobenzofuran (DPBF) as $^1O_2$ scavenger under the visible light (650 nm) irradiation. To a solution of DPBF (50 μM, 2 mL, DMSO), different quantities of Hal-PPIX and Hal-PPIX@Zn nanomaterial, were added (1.0 mg and 0.2 mg, respectively, corresponding to a sensitizer concentration of 0.02 mM in both cases). The obtained dispersions were transferred to a quartz tube and then stirred under laser irradiation at wavelength of 650 nm (200 mW). At predetermined time, the dispersion was centrifuged to remove the Hal based nanomaterials, and the supernatant solution was analyzed by UV–vis spectroscopy. The $^1O_2$ release was monitored by following the decrease in the absorbance spectrum of DPBF at 413 nm, during 20 min of irradiation. Thus, the singlet oxygen quantum yields for each nanomaterial were calculated, using methylene blue (MB, 10^{-5} M) as reference, according to the following equation:

$$\Phi\Delta\left(^1O_2\right)_n = \Phi\Delta\left(^1O_2\right)_{MB} \times \frac{S_n \times F_{MB}}{S_{MB} \times F_n} \quad (1)$$

where $\Phi\Delta(^1O_2)_n$ is the quantum yield of singlet oxygen for the two nanomaterials and $\Phi\Delta(^1O_2)_{MB}$ represents the quantum yield of singlet oxygen of MB ($\Phi\Delta(^1O_2)_{MB} = 0.52$ in DMSO). *S* is the slope of the plot of difference of absorbance of DPBF before and after irradiation at each time *t* considered (at 413 nm) (Fig. S5) with the irradiation time and *F* is the absorption correction factor, which is given by $F = 1–10^{-Abs}$ (Abs is the value of the absorbance at the irradiation wavelength of 650 nm).

2.9. Cell lines

HL-60R cells were cultured in Roswell Park Memorial Institute (RPMI) 1640 supplemented with 10 % heat inactivated fetal calf serum, 2 mM L-glutamine, 100 units/mL penicillin and 100 μg/mL streptomycin (all reagents were from HyClone Europe Ltd., Cramlington, UK) in a

humidified atmosphere at 37 °C in 5 % CO_2. HL-60 cells were obtained from ATCC® (CCL-240, Rockville, MD, USA), and were selected for multidrug resistance (MDR) by exposure to gradually increasing concentrations of doxorubicin.

2.10. Cell viability assays

Cells were seeded on 12-well plates at a density of 200,000 cells/well and incubated overnight at 37 °C. After 24 h, at time 0 the medium was replaced with a fresh complete medium and incubated with Hal-PPIX or Hal-PPIX@Zn. After 24 h of exposure, the cells were irradiated with laser for 5 min and incubated for further 4 h. Cells were seeded on 96-well plates in triplicates and incubated with 15 μL of Promega Corp. commercial solution (Madison, WI, USA) containing 3- (4,5-dimethylthiazol-2-yl) -5-(3-carboxymethoxyphenyl) -2-(4-sulfophenyl)-2H-tetrazolium (MTS) and phenazine ethosulfate. Using a microplate reader (iMark Microplate Reader; Bio-Rad Laboratories, Inc., Hercules, CA, USA) the bioreduction of the MTS dye was evaluated by measuring the absorbance of each well at 490 nm. Cytotoxicity was expressed as a percentage of measured absorbance relative to that of control cells.

2.11. Acridine orange staining assay

Cell suspensions were collected by centrifugation, washed thrice with PBS and then resuspended in 25 μL of dye (100 μg/mL of acridine orange prepared in PBS and mixed gently) for 10 min, washed thrice with PBS and immediately analyzed using a fluorescence microscope and examined under 40× magnification.

2.12. Statistical analysis

The statistical analysis of the experimental data was estimated using the statistical analysis software Past 4.03. All tests were performed in duplicate or triplicate (see infra), and the data were analyzed using a one-way analysis of variance (ANOVA). The significant difference values were tested using the Tukey test with a 95 % of confidence interval ($p < 0.05$). The results were displayed in the form of mean ± standard deviation.

2.13. Chitosan films preparation

Bionanocomposite films based on chitosan and Hal were prepared by the casting method. Chitosan at 2 wt% and an appropriate amount of Hal, Hal-PPIX or Hal-PPIX@Zn nanomaterial were dispersed in a 3 %*v*/v acetic acid solution; the polymer dispersions were kept under stirring overnight. The well-dispersed mixture was poured into different glass Petri dishes under vacuum at 60 °C up to 48 h in order to evaporate water solution of acetic acid until the weight was constant to obtain films. Dried biofilms contained 5 wt% of nanofiller.

3. Results and discussion

3.1. Synthesis, characterizations and properties of Hal-PPIX and Hal-PPIX@Zn nanomaterials

The covalent attachment of PPIX to Hal obtaining Hal-PPIX nanomaterial was successfully achieved via two different synthetic routes, microwave-assisted and UV irradiation, as depicted in Scheme 1. The first method involved the irradiation of a methanolic dispersion of previously synthetized thiolated halloysite (Hal-SH) (Massaro et al.,

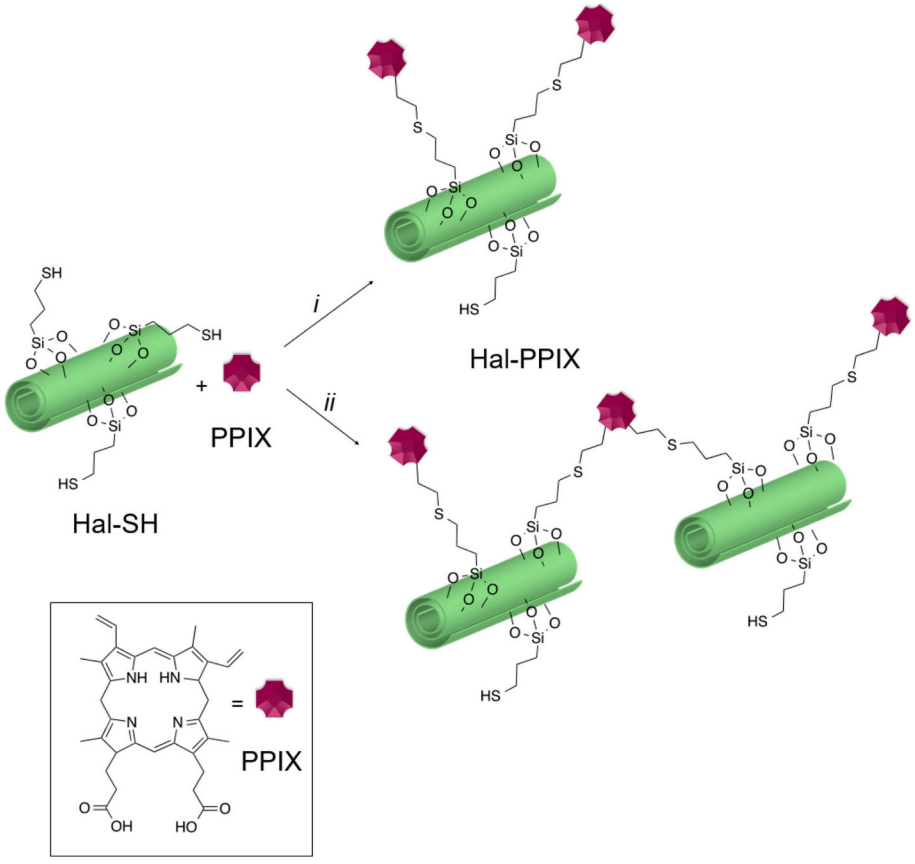

Scheme 1. Cartoon representation of the hypothesized structures of Hal-PPIX nanomaterials obtained with the two different pathways: (*i*) *hν*, MeOH, r.t., 24 h; (*ii*) AIBN, MW, 100 °C, 1 h solvent-free conditions.

2019) and PPIX with UV light from an Hg lamp at room temperature for 24 h (Massaro et al., 2015). The second method involved a microwave-assisted AIBN-catalyzed thiol-ene reaction between Hal-SH and PPIX, under solvent-free conditions at a temperature of 100 °C (Massaro et al., 2024b). After work-up, the loading percentage of PPIX on the Hal external surface was approximately 3.7 wt% for the AIBN catalyzed reaction and ca. 2.1 wt% and UV-catalyzed reaction, as estimated by thermogravimetric analysis (TGA). This indicates that the microwave assisted reaction was more advantageous in obtaining a higher loading of the organic portion onto the Hal surface than the conventional method.

Depending on the synthetic procedure, it was hypothesized that *i*) the allyl group of PPIX that do not react in the thiol-ene reaction can undergo a self-addition reaction, leading to the formation of more compact structure where the PPIX molecules can be linked together in the case of MW irradiation, *ii*) conversely, in the case of UV irradiation, they remain as free allyl groups available for further modifications, as already reported for other systems (Massaro et al., 2024b). This hypothesis was confirmed by morphological investigations, see *infra*. Based on the stoichiometric ratio after protoporphyrin IX attachment (with a functionalization degree of 0.16 mmol g^{-1} for thiol groups and 0.07 and 0.04 mmol g^{-1} for PPIX via MW and UV, respectively), it was determined that a full linkage of PPIX onto the thiol-modified Hal was not achieved, likely due to steric hindrance, leaving some -SH groups unreacted.

The successful synthesis was verified by TGA, FT-IR spectroscopy and XPS analyses. In this framework, the features of Hal-PPIX nanomaterial obtained by microwave irradiation were discussed. In all cases, similar considerations can be made for Hal-PPIX nanomaterial obtained under UV irradiation (see SI). Fig. 2a shows the thermogravimetric curves of Hal-SH and Hal-PPIX nanomaterials. Both samples exhibited two clear mass losses at 25–150 °C and 450–550 °C regions. The first mass loss (ML_{150}) reflects the moisture content of the materials as evidenced in literature for Hal modified with organic molecules (Cavallaro et al., 2023). As highlighted in Table 1, Hal-PPIX nanomaterial possesses a lower hydrophilic characteristic than Hal-SH precursor in agreement with the lower ML_{150} value. The second mass loss (ML_{500}) is due the

Table 1
Parameters (from TGA) of Hal-SH and Hal-PPIX nanomaterials.

Sample	ML150 / wt%	ML500 / wt%	ML600 / wt%
Hal-SH	1.9	10.0	83.3
Hal-PPIX	1.2	10.7	80.3

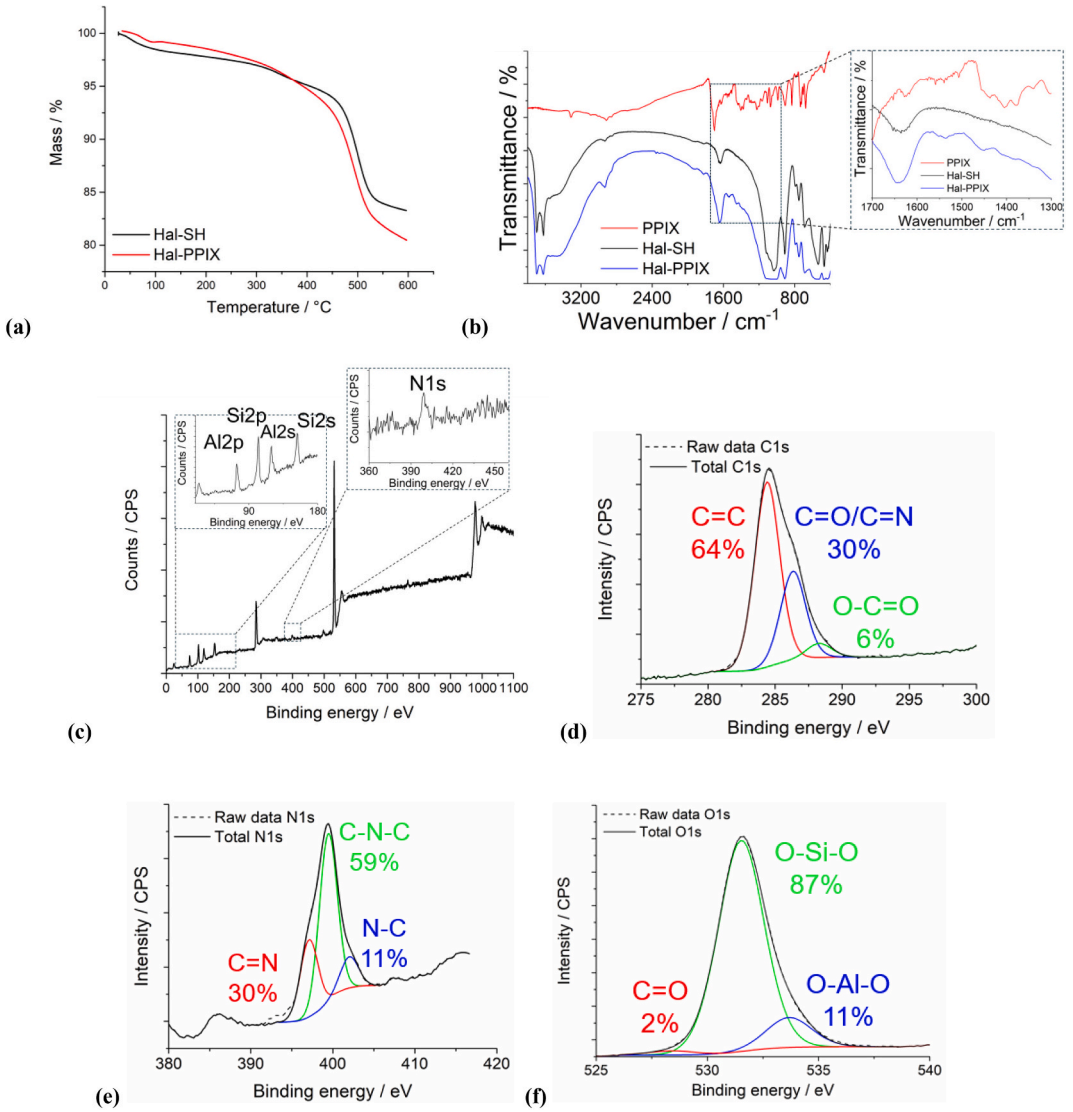

Fig. 2. (a)Thermogravimetric curves and (b) FT-IR spectra of PPIX, Hal and Hal-PPIX nanomaterials; (c) XPS survey of Hal-PPIX nanomaterial, (d) deconvoluted C 1 s spectrum; (e) deconvoluted N 1 s spectrum, (f) deconvoluted O 1 s spectrum.

expulsion of the two water molecules from the Hal interlayer (Calvino et al., 2024) and, partly, to PPIX decomposition, which occurs in a wide temperature range (300–500 °C) (Vadarevu et al., 2021). Accordingly, we cannot clearly discriminate the mentioned processes by thermogravimetric curves in the region 450–550 °C.

Thermogravimetric curves allowed us to estimate the PPIX amount grafted onto Hal-SH surface by considering the residual matters at 600 °C (MR_{600}). The similar ML_{600} values for Hal-SH and Hal-PPIX indicate that the surfaces modification did not alter the halloysite structural characteristics. According to the actual grafting of PPIX, the MR_{600} of Hal-PPIX nanomaterial was reduced as compared with Hal-SH (Table 1). On this basis, we calculated a functionalization degree of 3.7 wt% for PPIX nanomaterial. In Fig. 2b the FT-IR spectrum of Hal-PPIX nanomaterial and those of Hal-SH and PPIX for comparison are reported. As it is possible to observe, after the covalent linkage of PPIX onto Hal external surface, the FT-IR spectrum of Hal-PPIX nanomaterial showed characteristic vibrational features from both precursors.(Guo et al., 2016) As seen in the FT-IR spectra of Hal-PPIX, the bands at approximately 3602 and 3690 cm^{-1} correspond to the O—H stretching vibrations of the inner and outer hydroxyl groups of Hal, respectively. Additionally, the broad signal at 1640 cm^{-1} is attributed to the H–O–H bending of hydrogen-bonded water in the halloysite structure, which aligns with the broad O—H stretching signal observed at 3550 cm^{-1}. Furthermore, in the Hal-PPIX spectrum it can be possible to observe the vibration stretching bands in the wavenumber range 1540–1385 cm^{-1}, due to the stretching of C═C, C═N and, C—N groups of pyrazole moieties of PPIX (Dinache et al., 2023; Imanparast et al., 2022) and a broad band at ca. 1700 cm^{-1} that could be attributable to the stretching of carboxylic moieties of PPIX superimposed to that typical of Hal.

To further confirm the presence of different functional groups on the surface of the Hal-PPIX, XPS measurements were performed. Fig. 2c shows the XPS survey spectrum of Hal-PPIX. The spectrum reveals the presence of C, N, and O atoms, with peaks at 284.39 eV (C 1 s), 399.09 eV (N 1 s), and 531.64 eV (O 1 s). Additionally, peaks corresponding to Al 2 s, Al 2p, Si 2 s, and Si 2p are observed, indicating the presence of Hal. The percentages of C, N, and O atoms, as determined by XPS, are provided in Table S1. The high-resolution XPS spectrum of the C 1 s core (Fig. 2d) was deconvoluted into three components: sp^2 (C=C) at 284.40 eV, C=O/C=N at 286.33 eV, and O-C=O at 288.28 eV. The N 1 s spectrum (Fig. 2e) was deconvoluted into three peaks at 397.11, 399.44, and 402.03 eV, corresponding to C═N, C-N-C, and N—C, respectively. The O 1 s spectrum (Fig. 2f) was deconvoluted into three peaks at 528.8, 531.4, and 533.6 eV, which are attributed to C═O, O-Si-O, and O-Al-O groups, respectively.

Dynamic Light Scattering (DLS) measurements allow for the assessment of the structural properties of nanomaterials by analyzing their mobility in water and measuring the average translational diffusion coefficient. This coefficient reflects the size, shape, and hydration of the diffusing particles, along with any potential aggregation phenomena (Alfieri et al., 2022). The average diameter of an equivalent sphere can be calculated using the Stokes-Einstein equation, which serves as an indicator for tracking changes in particle size and interparticle aggregation. The Hal-PPIX nanomaterial showed a *Z*-average size similar to that of pristine Hal indicating a diffusion, in aqueous media, similar to that of halloysite (Table 2). The modification of halloysite external surface was also verified by ζ-potential measurements, that showed that Hal-PPIX possesses a ζ-potential value more negative than pristine Hal attributable to the presence of carboxylate moieties onto PPIX present at the Hal external surface (Table 1).

Table 2
Average hydrodynamic diameter and ζ-potential values for Hal and Hal-PPIX nanomaterials. Reported are the mean ± SD values of three independent experiments performed in triplicate.

Sample	Z-average size (nm)	ζ-potential (mV)
Hal	295 ± 16	−18 ± 1
Hal-PPIX[i]	471 ± 13	−22 ± 1
Hal-PPIX[ii]	293 ± 12	−25 ± 1

The structural features of the synthetized nanomaterials were observed by TEM and high-angle annular dark field scanning transmission electron microscopies (HAADF-STEM). TEM micrographs (Fig. 3A,E) clearly show the different morphologies of the nanomaterials obtained by the two synthetic approaches. Fig. 3A shows the morphology of the nanomaterial obtained by UV irradiation. As it is possible to observe the typical tubular structure of the Hal was preserved after grafting of protoporphyrin IX, where the organic molecules are uniformly distributed onto the Hal external surface, as shown by the elemental mapping, highlighting nitrogen atoms (Fig. 3B—C), extrapolated by energy-dispersive X-ray spectroscopy (EDS).

EDS measurements (Fig. 3D) also show the presence of C and N atoms, beside the typical elements of halloysite, corroborating the successful synthesis.

On the contrary, the Hal-PPIX nanomaterial obtained by MW irradiation, shows a well-organized structure (Fig. 3E). It was hypothesized that in addition to the thiol-ene reaction between the Hal-SH nanomaterial and PPIX, protoporphyrin IX may react with itself through an ene-ene reaction, bridging different tubes. The elemental mapping of N atoms shows that the latter are uniformly distributed on the Hal surface and between the different tubes in agreement with the presence of PPIX that links among different Hal (Figs. 3F and 3G).

To investigate the photoluminescence properties of Hal after the covalent bonding with PPIX, we analyzed their UV and fluorescence spectroscopic properties. In Fig. 4 the UV–*vis* extinction spectrum of a dispersion of Hal-PPIX nanomaterial in DMSO is reported, showing the typical absorption features of PPIX, namely it presents the Soret band at ca. 400 nm and four Q bands in the range 500–700 nm(Myrzakhmetov et al., 2021), although the latter are partially overlapped by the light scattering of the solid particles, which is responsible for spectral broadening (Rossi et al., 2008). In addition, the Soret band of the Hal-PPIX nanomaterial was red-shifted compared to free PPIX (Fig. S4), providing further evidence of the covalent attachment of the photosensitizer to the clay surface. This covalent linkage confines the PPIX near the external surface of Hal, which possesses acidic properties, (Massaro et al., 2022b) thereby shifting the maximum absorption band of PPIX toward higher wavelengths (Dar and Shah, 2020). Excitation of the dispersion results in strong triplet emission between 590 and 700 nm (maximum at 630 nm) in a similar way of sole PPIX (Fig. S4).

Porphyrins are known to complex with a wide range of metal cations, particularly divalent ones (Shao et al., 2019). The advantage of developing metalloporphyrins lies in the potential to enhance biological effects compared to metal-free porphyrins when used as photosensitizers in PDT. Therefore, before testing the ability of the developed nanomaterial as photosensitizer for potential PDT, its affinity for divalent metal ions was investigated by fluorescence titration using the Hal-PPIX nanomaterial obtained by MW irradiation. The emission spectrum of a Hal-PPIX nanomaterial methanolic dispersion was measured after excitation at 410 nm in the presence of varying concentrations of three metal ions: Co^{2+}, Cu^{2+} and Zn^{2+} ions. Although DMSO is the most effective solvent for dispersing the Hal-based nanomaterial and metal salts, in this case MeOH is preferred over DMSO due to the latter's strong coordination ability with metal ions (Orzeł et al., 2017). The results are shown in Fig. 4b-d. In all cases, fluorescence quenching of Hal-PPIX was observed, indicating that an interaction between the nanomaterial and the metal ions occurred. Interestingly, there was no shift in the emission wavelength of PPIX in Hal-PPIX nanomaterial, ruling out the formation of an exciplex, as reported in literature for studies on free PPIX molecules (Jhonsi et al., 2017). The fluorescence quenching of the Hal-PPIX nanomaterial was further analyzed using the Stern-Volmer equation at two different temperatures (20 and 37 °C):

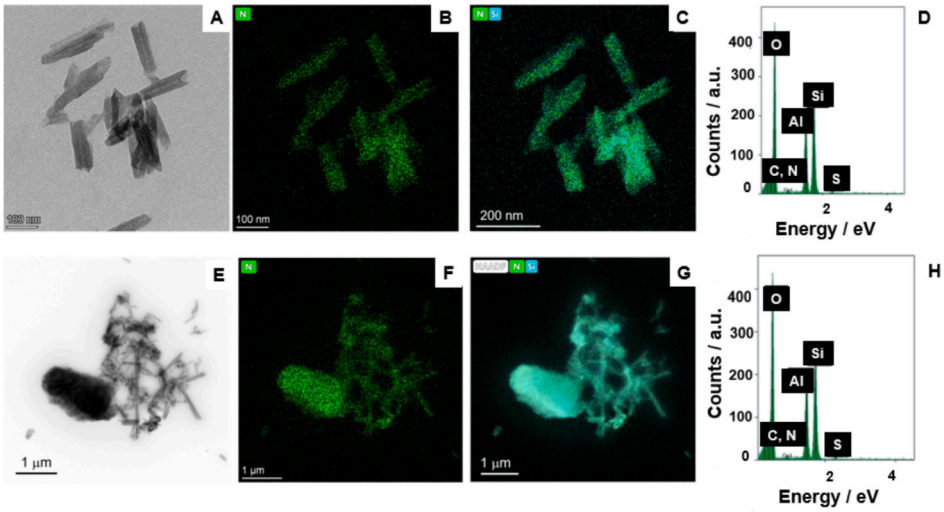

Fig. 3. (A-E) TEM image; (B—C, F-G) HAADF/STEM with elemental mapping images; (D—H) EDS analysis of Hal-PPIX nanomaterial obtained by (A-D) UV and (*E*-H) MW irradiation.

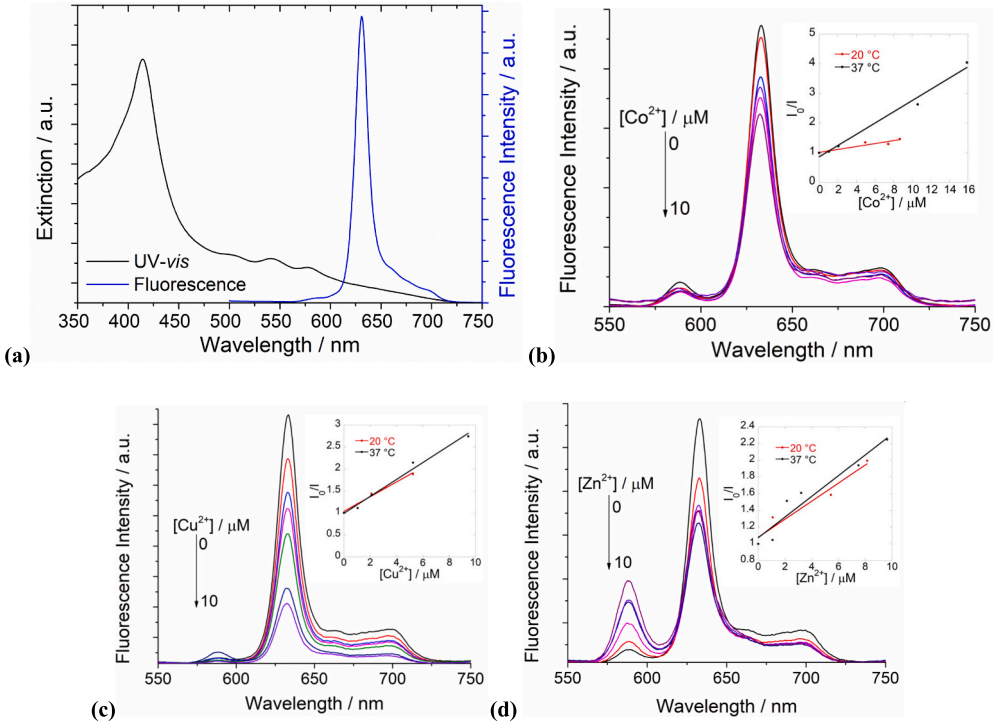

Fig. 4. (a) Extinction (black line) and emission (blue line) spectra of Hal-PPIX nanomaterial (1 mg mL^{-1}, DMSO, r.t.); (b-d) fluorescence trend of Hal-PPIX dispersion (0.1 mg mL^{-1}) upon addition of different concentrations of (b) Co^{2+}, (c) Cu^{2+} and (d) Zn^{2+} metal ions in methanol. The inset shows the Stern-Volmer plot of the Hal-PPX fluorescence in the presence of the metal ions at two different temperatures. (For interpretation of the references to colour in this figure legend, the reader is referred to the web version of this article.)

$$\frac{I_0}{I} = 1 + K_{SV} \bullet [Q] \quad (2)$$

where, I_0 and I are the fluorescence intensities of Hal-PPIX nanomaterial in the absence or presence of any metal ions, respectively, [Q] is the metal ions concentration and K_{SV} is the quenching constant. As shown in insets of Fig. 4b-d, the plot between I_0/I vs [Q], yielded a linear plot in all cases and by the fitting of experimental data it was found that the value of K_{SV} increases by increasing temperature indicating that the quenching process is dynamic (Table 3) (Deepa et al., 2020).

Based on these findings, it was possible to conclude that the

Table 3
K_{SV} of Co^{2+}, Cu^{2+} and Zn^{2+} ions quenching process at two different temperatures.

Metal ions	Temperature / °C	K_{sv} /10^5 M^{-1}
Co^{2+}	20	0.49
	37	1.89
Cu^{2+}	20	1.67
	37	1.92
Zn^{2+}	20	1.08
	37	1.24

Hal@PPIX nanomaterial showed a great affinity for metal ions allowing the synthesis of interesting nanomaterials with enhanced properties. Since Zn porphyrins have shown to be more efficient as photosensitizer in PDT than the metal-free porphyrin (Alea-Reyes et al., 2017), a new nanomaterial (Hal-PPIX@Zn) incorporating Zn^{2+} ions into Hal-PPIX, chosen as model, was synthetized and characterized. Firstly, the synthesis of PPIX@Zn was achieved through the complexation of PPIX with zinc chloride (Wang et al., 2023) which was subsequently reacted with Hal-SH as previously described, affording the Hal-PPIX@Zn nanomaterial (Fig. 5a). Also in this case, a thiol-ene reaction between thiol groups on Hal surface and the allyl ones of PPIX occurs affording the final nanomaterial. Because of the reactivity of Zn@PPIX is likely that this could be also subjected to a self-addition reaction, resulting in a more compact structure than that of the Hal-PPIX nanomaterial. The degree of functionalization was estimated to be 0.32 mmol g^{-1}, as determined by TGA (Fig. 5b).

The higher degree of functionalization in Hal-PPIX@Zn in comparison to the one of Hal-PPIX nanomaterial (0.07 mmol g^{-1}) resulted in different diffusion behaviors in water, as evidenced by DLS measurements. Specifically, a *Z*-average size of 1060 ± 60 nm was observed, indicating some aggregation phenomena. The successful modification was further verified by FT-IR spectroscopy (Fig. 5c). The photophysical properties showed that, similarly to that observed for Hal-PPIX nanomaterial, the Hal-PPIX@Zn one present the typical absorption and emission features of PPIX@Zn (Fig. 5d) (Peixoto et al., 2021). In particular, in the fluorescence spectrum of Hal-PPIX@Zn nanomaterial is clearly observable, beside the typical emission band of PPIX, an additional band related to the electron transfer between the metal and the porphyrin π system that are not influenced by the presence of Hal (Fig. S4).

Morphological studies of the Hal-PPIX@Zn nanomaterial revealed the presence of organized structures where the PPIX@Zn is uniformly distributed on the overall tube surface as shown by the EDX elemental mapping (Fig. 6). To verify that the PPIX and PPIX@Zn retained their

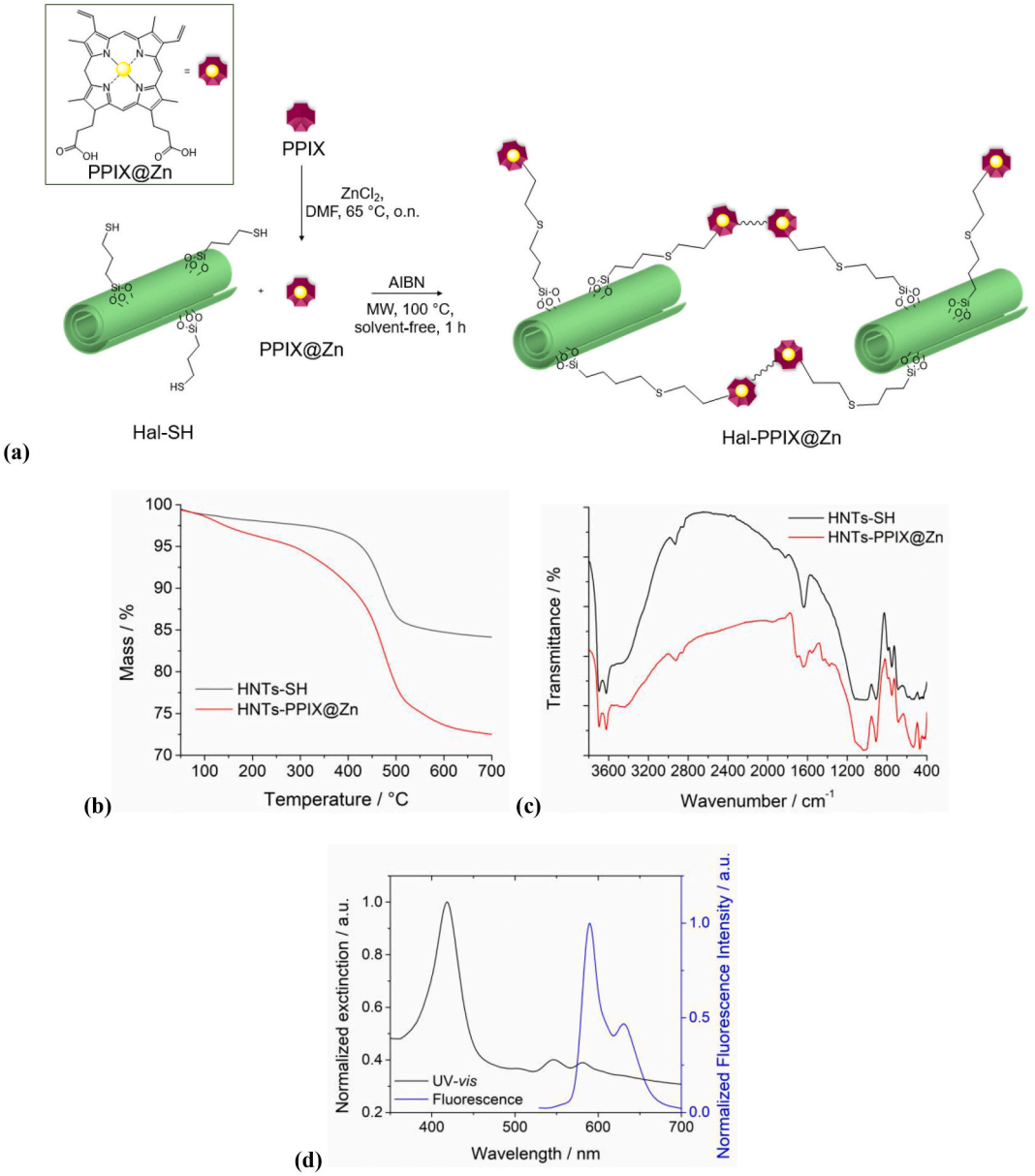

Fig. 5. (a) Cartoon representation of the hypothetic structures of Hal-PPIX@Zn nanomaterial; (b) TGA and (c) FT-IR spectra of Hal-SH and Hal-PPIX@Zn nanomaterials, (d) extinction (black line) and emission (blue line) spectra of Hal-PPIX@Zn nanomaterial (1 mg mL^{-1}, DMSO, r.t.). (For interpretation of the references to colour in this figure legend, the reader is referred to the web version of this article.)

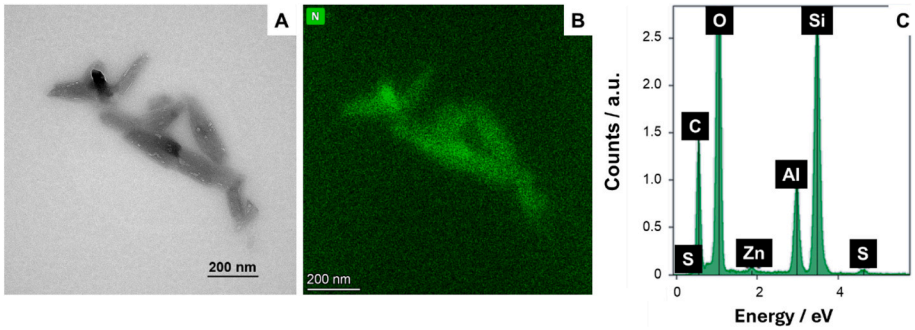

Fig. 6. (A) TEM image; (B) HAADF/STEM with elemental mapping images; (C) EDS analysis of Hal-PPIX@Zn nanomaterial.

photosensitizer properties after being linked to the Hal external surface, the generation of reactive oxygen species ($^1O_2$) by these nanomaterials was evaluated both chemically and biologically.

For a chemical point of view, preliminary studies were performed to investigate the ability of Hal-PPIX and Hal-PPX@Zn nanomaterials to produce $^1O_2$ using UV–*vis* spectroscopy. In particular, the changes in the UV–*vis* spectrum of 1,3-diphenylisobenzofuran (DPBF), a common $^1O_2$ scavenger, were monitored under laser irradiation (650 nm, 200 mW). Although porphyrins are most efficiently activated at the Soret band, this wavelength is less suitable for PDT due to significant light attenuation in the superficial tissue layers. Therefore, taking advantage of the presence of Q-bands in the 500–700 nm range, we selected a laser irradiation at 650 nm. As shown in Fig. 7a-b, the UV–*vis* absorbance intensity of DPBF in the presence of Hal-PPIX or Hal-PPIX@Zn nanomaterials (at concentration of 0.5 mg mL^{-1} and 0.1 mg mL^{-1}, respectively, corresponding to a sensitizer concentration of 0.02 mM in both cases) decreased under laser irradiation, indicating that the nanomaterials induced some effects. Conversely, the UV–*vis* absorption of the DPBF solution did not show any change under laser irradiation in absence of the nanomaterial. Similarly, no effects were observed in the presence of pristine Hal (Fig. 7c).

From the slope of the graph obtained by plotting the changes in absorbance of DPBF in the presence of Hal-PPIX and Hal-PPIX@Zn nanomaterials against irradiation time, the singlet oxygen quantum yields were calculated taking as reference methylene blue (MB) ($\Phi_\Delta(^1O_2)_{MB} = 0.52$ in DMSO) (Nagy-Simon et al., 2018; Stoean et al., 2024). Calculations gave $\Phi_\Delta(^1O_2)_{nanomaterial}$ of 0.20 and 0.45 for Hal-PPIX and Hal-PPIX@Zn, respectively, showing higher $^1O_2$ production from Hal-PPIX@Zn in comparison to Hal-PPIX (Hou et al., 2022).

From a biological point the view, to further evaluate the potential of the Hal based PPIX nanomaterials as photosensitizers, the multidrug resistant leukemia cell lines (HL-60R) were used as a model by MTS test in the absence or presence of light. These cells were selected because, being a suspension cell line, they could be irradiated more efficiently under the experimental conditions adopted. Additionally, as a drug-resistant cell line, they represent a more challenging model to assess the efficacy of the treatment. Finally, HL-60R cells have a relatively short doubling time (about 24 h), which makes them ideal for short-term experiments. Initially, the HL60R cells were incubated with the Hal-PPIX and Hal-PPIX@Zn nanomaterial for 24 h in dark conditions. As shown in Fig. 8a no significant impact on cells viability was observed, suggesting that both nanomaterials are biocompatible in the absence of light and can be utilized as potential photosensitizer for PDT (Semeraro et al., 2018). However, after laser irradiation (650 nm, 5 min, 200 mW) a notable phototoxicity effect was observed for both nanomaterials. Interestingly, the Hal-PPIX@Zn nanomaterial demonstrated a stronger photo-toxic response compared to Hal-PPIX, in agreement with the higher photodynamic properties of metalloporphyrins over metal-free

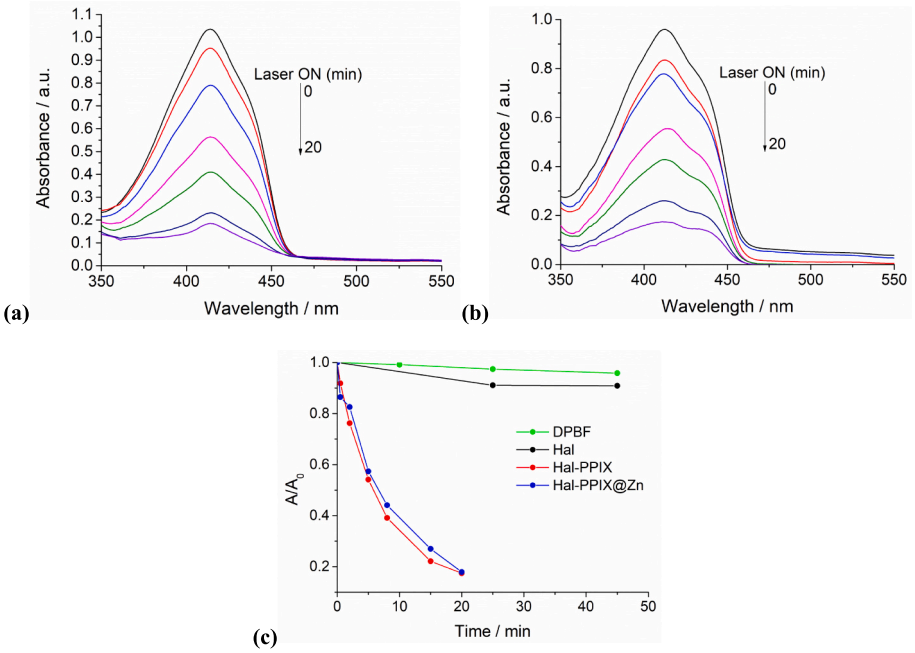

Fig. 7. Absorption spectra of DPBF and Hal-PPIX (a) or Hal-PPIX@Zn (b) dispersions in DMSO during sequential irradiations at 650 nm up to 20 min. (c) Plot of changes in DPBF absorbance at 413 nm against irradiation time in the absence (control) and in the presence of Hal, Hal-PPIX or Hal-PPIX@Zn in DMSO.

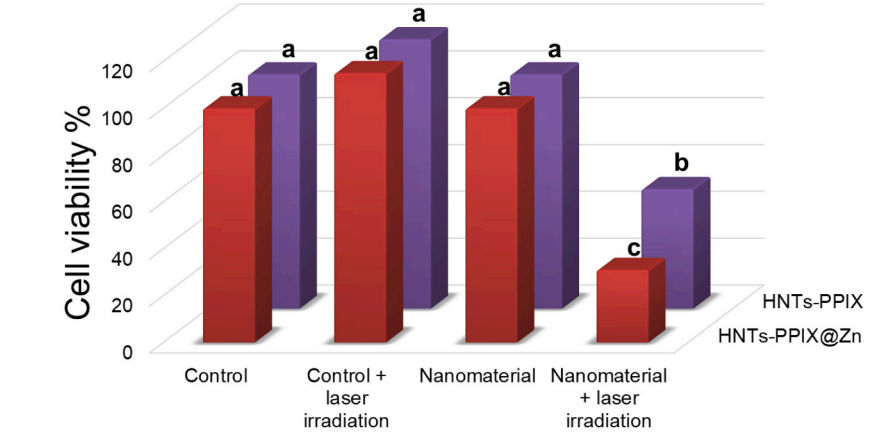

(a)

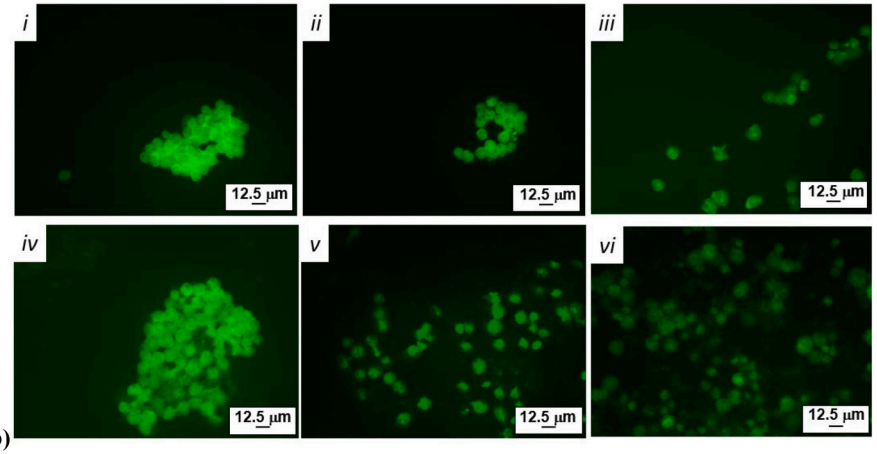

(b)

Fig. 8. (a) Evaluation of cytotoxicity after treatment with control, laser control, Hal-PPIX and Hal-PPIX@Zn nanomaterial under laser irradiation. The data represent the means ± standard deviations (SDs) of 3 independent experiments. In each graph, different letters above the columns indicate significant differences ($p < 0.05$) in cell viability; (b) Representative fluorescence microscopy images of morphological changes in HL-60R cell nuclei analyzed by acridine orange staining; (40× magnification); *i*) control, *ii*) laser control; *iii*) Hal-PPIX; *iv*) Hal-PPIX + laser; *v*) Hal-PPIX@Zn and *vi*) Hal-PPIX@Zn + laser.

porphyrins.

This confirmed once again that the inclusion on Zn^{2+} ions amplifies the efficiency of the photosensitizing effect, making Hal-PPIX@Zn a more potent option for PDT applications.

To further assess the antiproliferative activity of both Hal-PPIX and Hal-PPIX@Zn nanomaterials after laser irradiation, the cells morphological changes before and after laser irradiation were studies by their staining with acridine orange (Fig. 8b). As it is possible to observe from Figure 10b*i* cells of the control group, treated with laser (Fig. 8b*ii*) or with both Hal-PPIX (0.95 mg mL^{-1}) and Hal-PPIX@Zn (0.16 mg mL^{-1}) nanomaterials (Fig. 8b*iii* and 8b*v*) are alive and emitted a green fluorescence in a circular pattern showing an organized chromatin structure. Conversely, after laser irradiation (5 min) in the presence of the developed nanomaterials (Fig. 8b*iv* and 8b*vi*, respectively), early apoptotic cells were identified since they exhibit nuclear chromatin condensation as dense green spots, nuclear fragmentation and loss of membrane function.

3.2. Chitosan films: mechanical and morphological characterization

To explore the application of the synthesized nanomaterials in biomedical platforms, Hal-PPIX and Hal-PPIX@Zn were incorporated into chitosan films forming nanocomposites matrices. The incorporation of nanomaterials into chitosan films is vital for the future development of controlled delivery platforms for photosensitizers. This strategy enables localized application and enhances retention at the target site, potentially improving the precision and effectiveness of PDT.

The effects of the chitosan filling with Hal-PPIX and Hal-PPIX@Zn nanomaterials on the tensile performances of the biopolymeric film were investigated by Dynamic Mechanical Analysis (DMA). It should be noted that the concentration of the nanofiller was fixed at 5 wt%. Fig. 9 displays the stress vs strain curves of chitosan/Hal-PPIX and chitosan/Hal-PPIX@Zn nanocomposite films. Based on the analysis of stress vs strain curves, we calculated the tensile properties in terms of elastic modulus (E), stress at breaking point (σ_r) and ultimate elongation (ε_r). The data obtained were compared to those of chitosan and chitosan/Hal films (Table 4) We observed that chitosan/Hal-PPIX@Zn possesses the smallest values for all tensile parameters. The lowest value for the elastic modulus could be an indication of the highest flexibility in comparison with the other films. On the other hand, the addition of both Hal and Hal-PPIX generated negligible changes on *E* and σ_r of chitosan, while the ultimate elongation was significantly reduced. Additionally, Atomic Force Microscopy (AFM) (Fig. 10) was employed to investigate the surface morphology of the films, which is crucial for understanding the dispersion of nanomaterials within the chitosan matrix and their potential release behavior.

The topographical analysis performed on the thin film deposited by spin coated on silicon surface, exhibits the formation of a homogeneous

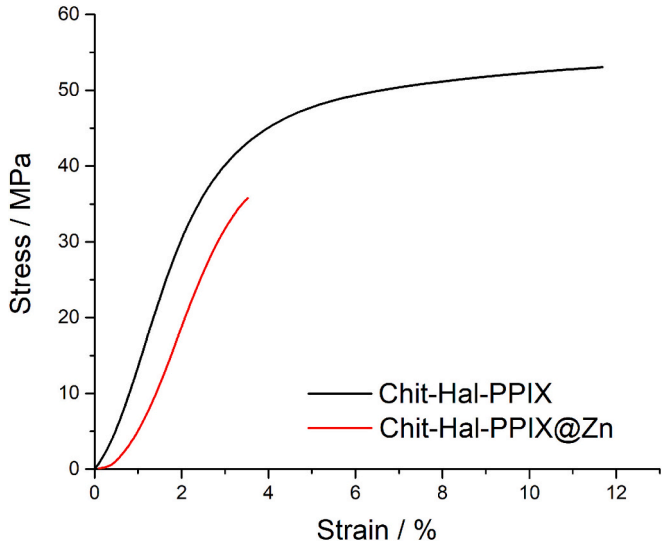

Fig. 9. (a) Stress vs strain curves for chitosan/Hal-PPIX and chitosan/HNT-PPIX@Zn nanocomposite films.

Table 4
Elastic modulus, stress at breaking point and ultimate elongation of Chitosan, Chitosan/Hal, Chitosan/Hal-PPIX and Chitosan/Hal-PPIX@Zn films.

Sample	*E* / MPa	σ_r / MPa	ε_r / %
Chitosan	1805	55.1	28.1
Chitosan/Hal	1785	54.1	12.1
Chitosan/Hal-PPIX	1799	56.1	11.6
Chitosan/Hal-PPIX@Zn	1327	35.7	3.5

layer of chitosan films and a uniform distribution of bare Hal, as well as functionalized ones onto surfaces (Fig. S6).

In particular, Fig. 10a shows the morphology of a thin layer of pristine chitosan on the surfaces. The addition of halloysite nanotubes within the chitosan film results in an increase layer thickness. Furthermore, as depicted in Fig. 10b, these nanotubes are observable at the interface, where they are slightly covered by the polymer matrix. It is important to mention that the influence of chitosan embedded with Hal-PPIX and Hal-PPIX@Zn is evident in the AFM height images, where the z range value (related to the film thickness) is greater than that observed in earlier samples. This observation likely arises from the strong interactions between the porphyrin- functionalized Hal and the chitosan, leading to a strong incorporation of the functionalized Hal within polymer matrix as reported in Fig. 10c-f. In conclusion, it is important to highlight that the 3D image of the Hal-PPIX@Zn film (Fig. 10f) shows small spikes on the external surface of the Hal. These spikes are likely a result of the immobilized zinc complex at the interface, thereby validating the successful surface functionalization of the Hal.

4. Conclusion

In this study, we developed chitosan-based nanocomposite films incorporating halloysite nanotubes covalently functionalized with Protoporphyrin IX (PPIX) and its Zn^{2+} complex (PPIX@Zn). The covalent anchoring strategy enabled stable integration of the photosensitizer onto the HNT surface, improving its solubility, dispersibility, and photodynamic performance. The resulting Hal-PPIX and Hal-PPIX@Zn nanomaterials efficiently generated singlet oxygen under visible light irradiation and exhibited phototoxic effects against multidrug-resistant leukemia cells (HL-60R), confirming their potential as light-activated therapeutic agents. When embedded in the chitosan matrix, the nanomaterials formed homogeneous, flexible films with tunable mechanical properties and well-defined surface morphology as confirmed by DMA and AFM, respectively. The functionalized Hal with protoporphyrin and its zinc complex induces a higher interaction with chitosan matrix inducing an increase in layer thickness. Moreover, the Hal-PPIX@Zn nanomaterial is visible in the morphology of the final nanocomposite, confirming the correct functionalization at interfaces. These results demonstrate the potential of Hal-based nanocomposites as effective, tunable systems for localized photodynamic therapy, with promising future applications in cancer treatment. These findings highlight the potential of covalently functionalized halloysite as a smart nanofiller for polysaccharide-based biomedical platforms. The proposed system represents a promising candidate for localized photodynamic therapy, particularly in the treatment of skin-related malignancies. Future work will focus on optimizing the nanocomposite formulation and evaluating its performance *in vivo* models.

CRediT authorship contribution statement

Marina Massaro: Writing – review & editing, Writing – original draft, Methodology, Investigation, Formal analysis. **Federica Leone:** Methodology, Investigation, Formal analysis. **Angelo Nicosia:**

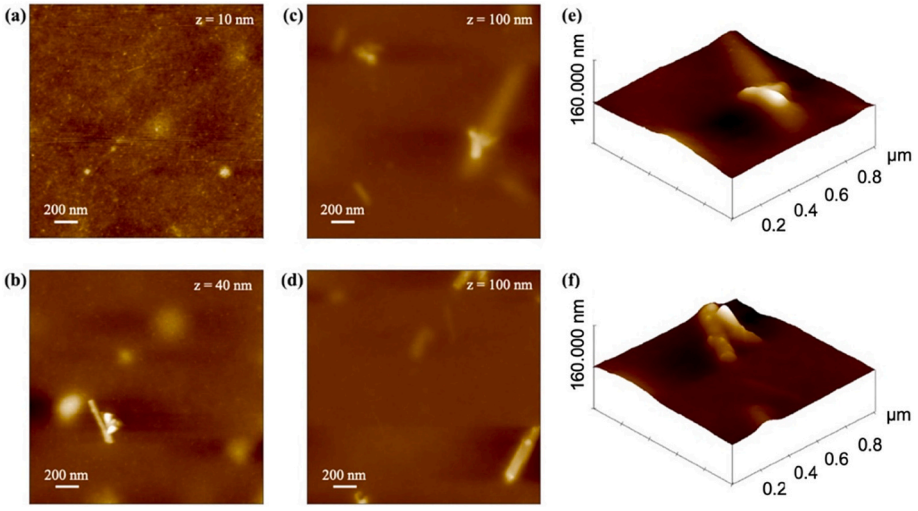

Fig. 10. Height atomic force microscopy image of (a) Chitosan, (b) Chitosan/Hal, (c) Chitosan/Hal-PPIX, (d) Chitosan/Hal-PPIX@Zn films, (e) 3D images of Chitosan/Hal-PPIX, (f) Chitosan/Hal-PPIX@Zn films.

Methodology, Investigation, Formal analysis. **Giuseppe Lazzara:** Writing – original draft, Methodology, Formal analysis. **Giuseppe Cavallaro:** Writing – original draft, Methodology, Investigation, Formal analysis. **Grazia M.L. Messina:** Writing – original draft, Methodology, Investigation, Formal analysis. **César Viseras:** Resources, Formal analysis. **Rita Sánchez-Espejo:** Methodology, Formal analysis. **Monica Notarbartolo:** Writing – original draft, Methodology, Investigation, Formal analysis. **Roberta Puglisi:** Methodology, Formal analysis. **Placido G. Mineo:** Writing – original draft, Methodology, Formal analysis. **Raquel de Melo Barbosa:** Resources, Methodology, Formal analysis. **Serena Riela:** Writing – review & editing, Writing – original draft, Supervision, Resources, Methodology, Formal analysis, Conceptualization.

Declaration of competing interest

The authors declare that they have no known competing financial interests or personal relationships that could have appeared to influence the work reported in this paper.

Acknowledgements

F.L. is gratefully to Avviso 01/2022 – Borse regionali di ricerca in Sicilia A.A 2022/2023 – CUP: G71I22001190006 for funding her PhD scholarship. XPS analysis was performed at ATeN Center-University of Palermo. Authors are thankful for the support offered by the Spanish Project PID2022-137603013-100 (Ministerio de Ciencia, Innovación y Universidades) and EMERGIA Program Project 2022/00001046 (Junta de Andalucía). This work was supported by National Recovery and Resilience Plan (NRRP), funded by the European Union– Next Generation EU-DD 1409 Progetti di Rilevante Interesse Nazionale (PRIN) 2022 PNRR published on 14-09-2022 by the italian MUR, Missione 4 (Istruzione e Ricerca) Component 2, Investment 1.1. Project Title: Small Molecule Anticancer Ligands Library from mediterranean plants (SMALL)– CUPB53D23025910001–Code P2022YJZ5F; and Linea di Intervento 1 Progetti di Ricerca Collaborativa del "PIAno di inCEntivi per la RIcerca di Ateneo 2024/2026" of University of Catania with the project "the project Sviluppo di nanobiopesticidi basati su argille minerali per applicazioni in agricoltura".

Appendix A. Supplementary data

Supplementary data to this article can be found online at https://doi.org/10.1016/j.clay.2025.107942.

Data availability

No data was used for the research described in the article.

References

Alea-Reyes, M.E., Soriano, J., Mora-Espí, I., Rodrigues, M., Russell, D.A., Barrios, L., Pérez-García, L., 2017. Amphiphilic gemini pyridinium-mediated incorporation of Zn(II)meso-tetrakis(4-carboxyphenyl)porphyrin into water-soluble gold nanoparticles for photodynamic therapy. Colloids Surf. B: Biointerfaces 158, 602–609.

Alfieri, M.L., Massaro, M., d'Ischia, M., D'Errico, G., Gallucci, N., Gruttadauria, M., Licciardi, M., Liotta, L.F., Nicotra, G., Sfuncia, G., Riela, S., 2022. Site-specific halloysite functionalization by polydopamine: a new synthetic route for potential near infrared-activated delivery system. J. Colloid Interface Sci. 606, 1779–1791.

Almeida, E.D.P., Santos Silva, L.A., de Araujo, G.R.S., Montalvão, M.M., Matos, S.S., da Cunha Gonsalves, J.K.M., de Souza Nunes, R., de Meneses, C.T., Oliveira Araujo, R. G., Sarmento, V.H.V., De Lucca, W., Correa, C.B., Rodrigues, J.J., Lira, A.A.M., 2022. Chitosan-functionalized nanostructured lipid carriers containing chloroaluminum phthalocyanine for photodynamic therapy of skin cancer. Eur. J. Pharm. Biopharm. 179, 221–231.

Bao, Z., Yan, Y., Han, W., 2024. Investigation of γ-aminopropyltriethoxysilane (APTES)-modified halloysite nanotubes on the reinforcement of halloysite/polypropylene (PP) nanocomposites. Polymers 16, 3332.

Bertolino, V., Cavallaro, G., Lazzara, G., Merli, M., Milioto, S., Parisi, F., Sciascia, L., 2016. Effect of the biopolymer charge and the nanoclay morphology on nanocomposite materials. Ind. Eng. Chem. Res. 55, 7373–7380.

Boraei, S.B.A., Eshghabadi, F., Hosseinpour, R., Zare, Y., Munir, M.T., Rhee, K.Y., 2024. Halloysite nanotubes in biomedical applications: recent approaches and future trends. Appl. Clay Sci. 253, 107346.

Calvino, M.M., Cavallaro, G., Milioto, S., Lazzara, G., 2024. Composite materials based on halloysite clay nanotubes and cellulose from *Posidonia oceanica* sea balls: from films to geopolymers. Environ. Sci. Nano 11, 1508–1520.

Cavallaro, G., Lazzara, G., Milioto, S., 2023. Nanocomposites based on halloysite nanotubes and sulphated galactan from red seaweed gloiopeltis: properties and delivery capacity of sodium diclofenac. Int. J. Biol. Macromol. 234, 123645.

Chen, C., Wu, C., Yu, J., Zhu, X., Wu, Y., Liu, J., Zhang, Y., 2022. Photodynamic-based combinatorial cancer therapy strategies: tuning the properties of nanoplatform according to oncotherapy needs. Coord. Chem. Rev. 461, 214495.

da Silva, C.L., Del Ciampo, J.O., Rossetti, F.C., Bentley, M.V.L.B., Pierre, M.B.R., 2013. Improved in vitro and in vivo cutaneous delivery of protoporphyrin IX from PLGA-based nanoparticles. Photochem. Photobiol. 89, 1176–1184.

Dar, U.A., Shah, S.A., 2020. UV–visible and fluorescence spectroscopic assessment of meso-tetrakis-(4-halophenyl) porphyrin; H2TXPP (X = F, Cl, Br, I) in THF and THF-water system: effect of pH and aggregation behaviour. Spectrochim. Acta, Pt. A: Mol. Biomol. Spectrosc. 240, 118570.

Deepa, H.R., Thipperudrappa, J., Suresh Kumar, H.M., 2020. Effect of temperature on fluorescence quenching and emission characteristics of laser dyes. J. Phys. Conf. Ser. 1473, 012046.

Dinache, A., Nistorescu, S., Tozar, T., Smarandache, A., Boni, M., Prepelita, P., Staicu, A., 2023. Spectroscopic investigations of porphyrin-TiO2 nanoparticles complexes. Molecules 28, 318.

Ding, H., Sumer, B.D., Kessinger, C.W., Dong, Y., Huang, G., Boothman, D.A., Gao, J., 2011. Nanoscopic micelle delivery improves the photophysical properties and efficacy of photodynamic therapy of protoporphyrin IX. J. Control. Release 151, 271–277.

Falanga, A.P., Massaro, M., Borbone, N., Notarbartolo, M., Piccialli, G., Liotta, L.F., Sanchez-Espejo, R., Viseras Iborra, C., Raymo, F.M., Oliviero, G., Riela, S., 2024. Carrier capability of halloysite nanotubes for the intracellular delivery of antisense PNA targeting mRNA of neuroglobin gene. J. Colloid Interface Sci. 663, 9–20.

Feng, Y., Chen, X., He, R.-R., Liu, Z., Lvov, Y.M., Liu, M., 2024. The horizons of medical mineralogy: structure-bioactivity relationship and biomedical applications of halloysite nanoclay. ACS Nano 18, 20001–20026.

Guo, J., Wang, Y., Wang, J., Zheng, X., Chang, D., Wang, S., Jiang, T., 2016. A novel nanogel delivery of poly-α, β-polyasparthydrazide by reverse microemulsion and its redox-responsive release of 5-fluorouridine. Asian J. Pharm. Sci. 11, 735–743.

Hou, B., Zhang, W., Li, C., Sun, X., Feng, X., Liu, J., 2022. Synthesis and in vitro biological evaluation of novel water-soluble porphyrin complexes for cancer photodynamic therapy. Appl. Organomet. Chem. 36, e6598.

Husain, T., Shoaib, M.H., Ahmed, F.R., Yousuf, R.I., Siddiqui, F., Saleem, M.T., Farooqi, S., Jabeen, S., 2023. Halloysite nanotubes-cellulose ether based biocomposite matrix, a potential sustained release system for BCS class I drug verapamil hydrochloride: compression characterization, in-vitro release kinetics, and in-vivo mechanistic physiologically based pharmacokinetic modeling studies. Int. J. Biol. Macromol. 251, 126409.

Imanparast, A., Attaran, N., Eshghi, H., Sazgarnia, A., 2022. Surface modification of gold nanoparticles with 6-mercapto-1-hexanol to facilitate dual conjugation of protoporphyrin IX and folic acid for improving the targeted photochemical internalization. Iran. J. Basic Med. Sci. 25, 970–979.

Izquierdo, N., Gamez, E., Alejo, T., Mendoza, G., Arruebo, M., 2024. Antimicrobial photodynamic therapy using encapsulated protoporphyrin IX for the treatment of bacterial pathogens. Materials 17, 1717.

Jabeen, N., Atif, M., 2024. Polysaccharides based biopolymers for biomedical applications: a review. Polym. Adv. Technol. 35, e6203.

Jhonsi, M.A., Nithya, C., Kathiravan, A., 2017. Unravel the interaction of protoporphyrin IX with reduced graphene oxide by vital spectroscopic techniques. Spectrochim. Acta Pt. A Mol. Biomol. Spectrosc. 178, 86–93.

Karewicz, A., Machowska, A., Kasprzyk, M., Ledwójcik, G., 2021. Application of halloysite nanotubes in cancer therapy—a review. Materials 14, 2943.

Khan, M.M., Madni, A., Filipczak, N., Pan, J., Rehman, M., Rai, N., Attia, S.A., Torchilin, V.P., 2020. Folate targeted lipid chitosan hybrid nanoparticles for enhanced anti-tumor efficacy. Nanomedicine 28, 102228.

Li, L.-Y., Zhou, Y.-M., Gao, R.-Y., Liu, X.-C., Du, H.-H., Zhang, J.-L., Ai, X.-C., Zhang, J.-P., Fu, L.-M., Skibsted, L.H., 2019. Naturally occurring nanotube with surface modification as biocompatible, target-specific nanocarrier for cancer phototherapy. Biomaterials 190-191, 86–96.

Massaro, M., Piana, S., Colletti, C.G., Noto, R., Riela, S., Baiamonte, C., Giordano, C., Pizzolanti, G., Cavallaro, G., Milioto, S., Lazzara, G., 2015. Multicavity halloysite–amphiphilic cyclodextrin hybrids for co-delivery of natural drugs into thyroid cancer cells. J. Mater. Chem. B 3, 4074–4081.

Massaro, M., Colletti, C.G., Fiore, B., La Parola, V., Lazzara, G., Guernelli, S., Zaccheroni, N., Riela, S., 2019. Gold nanoparticles stabilized by modified halloysite nanotubes for catalytic applications. Appl. Organomet. Chem. 33, e4665.

Massaro, M., Viseras Iborra, C., Cavallaro, G., Colletti, C.G., García-Villén, F., Lazzara, G., Riela, S., 2021. Synthesis and characterization of nanomaterial based on halloysite and hectorite clay minerals covalently bridged. Nanomaterials 11, 506.

Massaro, M., Licandro, E., Cauteruccio, S., Lazzara, G., Liotta, L.F., Notarbartolo, M., Raymo, F.M., Sánchez-Espejo, R., Viseras-Iborra, C., Riela, S., 2022a. Nanocarrier based on halloysite and fluorescent probe for intracellular delivery of peptide nucleic acids. J. Colloid Interface Sci. 620, 221–233.

Massaro, M., Notarbartolo, M., Raymo, F.M., Cavallaro, G., Lazzara, G., Mazza, M.M.A., Viseras-Iborra, C., Riela, S., 2022b. Supramolecular association of halochromic switches and halloysite nanotubes in fluorescent nanoprobes for tumor detection. ACS Appl. Nano Mater. 5, 13729–13736.

Massaro, M., Poma, P., Cavallaro, G., García-Villén, F., Lazzara, G., Notarbartolo, M., Muratore, N., Sánchez-Espejo, R., Viseras Iborra, C., Riela, S., 2022c. Prodrug based on halloysite delivery systems to improve the antitumor ability of methotrexate in leukemia cell lines. Colloids Surf. B: Biointerfaces 213, 112385.

Massaro, M., Ghersi, G., de Melo Barbosa, R., Campora, S., Rigogliuso, S., Sànchez-Espejo, R., Viseras-Iborra, C., Riela, S., 2023. Nanoformulations based on collagenases loaded into halloysite/Veegum® clay minerals for potential pharmaceutical applications. Colloids Surf. B: Biointerfaces 230, 113511.

Massaro, M., Ciani, R., Grossi, G., Cavallaro, G., de Melo Barbosa, R., Falesiedi, M., Fortuna, C.G., Carbone, A., Schenone, S., Sánchez-Espejo, R., Viseras, C., Vago, R., Riela, S., 2024a. Halloysite nanotube-based delivery of pyrazolo[3,4-d]pyrimidine derivatives for prostate and bladder cancer treatment. Pharmaceutics 16.

Massaro, M., Pettignano, A., Muratore, N., Fusteș-Dămoc, I., Cavallaro, G., Lazzara, G., Meo, P.L., Mija, A., Sánchez-Espejo, R., Viseras Iborra, C., Riela, S., 2024b. Cyclodextrin-grafted-hectorite based nanomaterial for antibiotics and metal ions adsorption. Appl. Clay Sci. 250, 107271.

Moura, D., Mano, J.F., Paiva, M.C., Alves, N.M., 2016. Chitosan nanocomposites based on distinct inorganic fillers for biomedical applications. Sci. Technol. Adv. Mater. 17, 626–643.

Myrzakhmetov, B., Arnoux, P., Mordon, S., Acherar, S., Tsoy, I., Frochot, C., 2021. Photophysical properties of protoporphyrin IX, pyropheophorbide-a, and photofrin® in different conditions. Pharmaceuticals 14, 138.

Nagy-Simon, T., Potara, M., Craciun, A.M., Licarete, E., Astilean, S., 2018. IR780-dye loaded gold nanoparticles as new near infrared activatable nanotheranostic agents for simultaneous photodynamic and photothermal therapy and intracellular tracking by surface enhanced resonant Raman scattering imaging. J. Colloid Interface Sci. 517, 239–250.

Nicosia, A., Vento, F., Satriano, C., Villari, V., Micali, N., Cucci, L.M., Sanfilippo, V., Mineo, P.G., 2020. Light-triggered polymeric nanobombs for targeted cell death. ACS Appl. Nano Mater. 3, 1950–1960.

Nikezić, A.V.V., Bondžić, A.M., Vasić, V.M., 2020. Drug delivery systems based on nanoparticles and related nanostructures. Eur. J. Pharm. Sci. 151, 105412.

Orzeł, Ł., Waś, J., Kania, A., Susz, A., Rutkowska-Zbik, D., Staroń, J., Witko, M., Stochel, G., Fiedor, L., 2017. Factors controlling the reactivity of divalent metal ions towards pheophytin a. JBIC J. Biol. Inorg. Chem. 22, 941–952.

Peixoto, D., Pereira, I., Pereira-Silva, M., Veiga, F., Hamblin, M.R., Lvov, Y., Liu, M., Paiva-Santos, A.C., 2021. Emerging role of nanoclays in cancer research, diagnosis, and therapy. Coord. Chem. Rev. 440, 213956.

Penon, O., Marín, M.J., Russell, D.A., Pérez-García, L., 2017. Water soluble, multifunctional antibody-porphyrin gold nanoparticles for targeted photodynamic therapy. J. Colloid Interface Sci. 496, 100–110.

Rossi, L.M., Silva, P.R., Vono, L.L.R., Fernandes, A.U., Tada, D.B., Baptista, M.S., 2008. Protoporphyrin IX nanoparticle carrier: preparation, optical properties, and singlet oxygen generation. Langmuir 24, 12534–12538.

Semeraro, P., Chimienti, G., Altamura, E., Fini, P., Rizzi, V., Cosma, P., 2018. Chlorophyll a in cyclodextrin supramolecular complexes as a natural photosensitizer for photodynamic therapy (PDT) applications. Mater. Sci. Eng. C 85, 47–56.

Shao, S., Rajendiran, V., Lovell, J.F., 2019. Metalloporphyrin nanoparticles: coordinating diverse theranostic functions. Coord. Chem. Rev. 379, 99–120.

Silva, A.O., Cunha, R.S., Hotza, D., Machado, R.A.F., 2021. Chitosan as a matrix of nanocomposites: a review on nanostructures, processes, properties, and applications. Carbohydr. Polym. 272, 118472.

Stoean, B., Lupan, I., Cristea, C., Silion, M., Silaghi-Dumitrescu, L., Silaghi-Dumitrescu, R., Gaina, L.I., 2024. Outcomes of folic acid esterification upon the properties of hydrophilic phenothiazinium dyes: new photosensitizers for antimicrobial photodynamic therapy. J. Photochem. Photobiol. A Chem. 451, 115500.

Tan, C., Zheng, J., Feng, Y., Liu, M., 2021. Cell membrane-coated halloysite nanotubes for target-specific nanocarrier for cancer phototherapy. Molecules 26, 4483.

Thomas, J., Selvin Thomas, P., Stephen, R., 2024. Improved mechanical, thermal, and barrier properties of halloysite nanotubes and nanocellulose incorporated PVA-PEO films: for food packaging applications. Food Packag. Shelf Life 46, 101373.

Vadarevu, H., Juneja, R., Lyles, Z., Vivero-Escoto, J.L., 2021. Light-activated protoporphyrin IX-based polysilsesquioxane nanoparticles induce ferroptosis in melanoma cells. Nanomaterials 11, 2324.

Villari, V., Micali, N., Nicosia, A., Mineo, P., 2021. Water-soluble non-ionic PEGylated porphyrins: a versatile category of dyes for basic science and applications. Top. Curr. Chem. 379, 35.

Wang, D., Ma, L., Wang, D., Wang, R., Wang, N., Li, J., 2023. Zinc(II) porphyrin-based ionic porous organic polymers (iPOPs) having abundant dual-function sites for promoting cycloaddition of CO2 with epoxides. Appl. Catal. A Gen. 665, 119380.

Yadav, M., Kaushik, B., Rao, G.K., Srivastava, C.M., Vaya, D., 2023. Advances and challenges in the use of chitosan and its derivatives in biomedical fields: a review. Carbohydr. Polym. Technol. Appl. 5, 100323.

Yanamadala, Y., Saleh, M.Y., Williams, A.A., Lvov, Y., Murray, T.A., 2023. Clay nanotubes loaded with diazepam or xylazine permeate the brain through intranasal administration in mice. Int. J. Mol. Sci. 24, 9648.

Yang, C., Wang, K., Liang, G., Tian, S., Peng, J., Mo, L., Lin, W., 2023. A versatile MOF-derived theranostic for dual-miRNA controlled accurate cancer cell recognition and photodynamic therapy. Talanta 265, 124805.